catalysts

MDPI

Article

Preparation and Electrocatalytic Properties of One-Dimensional Nanorod-Shaped N, S Co-Doped Bimetallic Catalysts of FeCuS-N-C

Hong Shi [1], Lina Wu [2,*], Qi Zhang [1], Yizhou Zhang [1], Wentao Sun [1], Chunbo Liu [3] and Rongxian Zhang [1,*]

[1] School of Chemistry and Chemical Engineering, Jiangsu University, Zhenjiang 212013, China; hshi@ujs.edu.cn (H.S.); 19708898575@163.com (Q.Z.); zhou304777@163.com (Y.Z.); sunwentao321@gmail.com (W.S.)
[2] College of Chemistry, Baicheng Normal University, Baicheng 137000, China
[3] Jilin Joint Technology Innovation Laboratory of Developing and Utilof Developing and Utilizing Materials of Reducing Pollution and Carbon Emissions, College of Engineering, Jilin Normal University, Siping 136000, China; chunboliu@jlnu.edu.cn (C.L.)
* Correspondence: wuln@bcnu.edu.cn (L.W.); rong@ujs.edu.cn (R.Z.)

Abstract: Metal air batteries have gradually attracted public attention due to their advantages such as high power density, high energy density, high energy conversion efficiency, and clean and green products. Reasonable design of oxygen reduction reaction (ORR) catalysts with high cost-effectiveness, high activity, and high stability is of great significance. Metal organic frameworks (MOFs) have the advantages of large specific surface area, high porosity, and designability, which make them widely used in many fields, especially in catalysis. This paper starts with regulating and optimizing the composition and structure of MOFs. A series of N, S co-doped electrocatalysts FeCuS-N-C were prepared by two high-temperature pyrolysis processes using N-doped carbon hollow nanorods derived from ZIF-8 as the substrate. The one-dimensional nanorod material derived from this MOF exhibits excellent electrocatalytic ORR performance (Eonset = 0.998 V, $E_{1/2}$ = 0.874 V). When used as the air cathode catalyst for zinc air batteries and assembled into liquid ZABs, the battery discharge curve was calculated and found to have a maximum power density of 142.7 mW cm^{-2}, a specific capacity of 817.1 mAh gZn^{-1}, and a cycling stability test of over 400 h. This study provides an innovative approach for designing and optimizing non-precious metal catalysts for zinc air batteries.

Keywords: metal–organic frameworks; Zn-air battery; oxygen reduction reaction; electrocatalysts

Citation: Shi, H.; Wu, L.; Zhang, Q.; Zhang, Y.; Sun, W.; Liu, C.; Zhang, R. Preparation and Electrocatalytic Properties of One-Dimensional Nanorod-Shaped N, S Co-Doped Bimetallic Catalysts of FeCuS-N-C. *Catalysts* **2024**, *14*, 849. https://doi.org/10.3390/catal14120849

Academic Editors: Jose L. Diaz De Tuesta and Fernanda Fontana Roman

Received: 29 October 2024
Revised: 15 November 2024
Accepted: 20 November 2024
Published: 23 November 2024

1. Introduction

Zn-air batteries (ZABs) have become an ideal solution for solving problems such as fossil fuel shortage and environmental degradation due to their advantages of high energy density, environmental friendliness, and abundant zinc sources. They are considered as a strong candidate for the next generation of energy storage devices [1–4]. The discharge performance and stability of ZABs are closely related to the kinetics of oxygen reduction reaction (ORR) on the cathode side, and the four-electron reaction process of ORR is highly dependent on the catalytic performance of catalysts on the cathode side [5,6]. Developing efficient and low-cost catalysts for the four-electron reaction is an urgent need for ZABs [7]. However, the high energy demand for O=O bond breaking and 4 $e^-/4H^+$ transfer process results in suboptimal ORR performance for most catalysts [8,9]. Although catalysts based on platinum group metals (PGMs) have shown the most advanced activity in ORR, their large-scale commercial applications are limited by their high cost and scarcity [10,11]. In the past few decades, a large number of carbon-based non-precious metal catalysts have been developed and explored as the most promising alternatives, among which transition metal nitrogen carbon materials (M–N–C, M=Fe, Co, Cu, Ni, Mn, etc.) have the highest atomic utilization rate and lower cost, and are considered to be the most promising catalysts to replace PGM materials [12–14]. The coordinated nitrogen atom can regulate the electron cloud density of transition metals, and optimize the adsorption and desorption of intermediates [15–17]. Meanwhile, transition metal atoms and nitrogen atoms can form M-N_x species, which are synergistic active sites for ORR [18,19]. Among transition metal nitrogen carbon catalysts, Fe-N-C catalysts exhibit the maximum potential for commercial applications in ZABs, where the initial potential and half-wave potential are equivalent to 20%of the PGM electrocatalysts in alkaline systems [20,21]. However, further improving the electrocatalytic activity and durability of Fe-N-C catalysts by adjusting their electronic and morphological structures to meet practical applications remains a huge challenge [22–24].

The stability degradation of Fe-N-C catalysts is mainly due to the oxidation of carbon substrates and poisoning of the active site Fe-N_x. In recent years, double single atom catalysts (DSACs) with bimetallic active sites have been prepared by introducing a second type of transition metal (Co, Mn, Cu, etc.) and non-metallic elements (B, P, S, etc.). The M-d band centers of the planar M-N_4 structure dispersed in the carbon lattice have been optimized, which can effectively regulate the electronic structure of the active sites, optimize their adsorption strength with intermediate products, accelerate the cleavage of O=O bonds, and thereby improve ORR activity [5,25]. As reported by Wu et al. [26], Fe and Co single atoms are stabilized on two-dimensional carbon nanosheets by coordinating with nitrogen (N) and sulfur (S) heteroatoms, forming a FeN_4S_1/CoN_4S_1 configuration. Compared with single atoms, the synergistic effect between Fe and Co double single atoms can reduce the absorption/desorption energy barrier of intermediates, enhance charge transfer, and achieve stable and superior ORR activity of the catalyst.

Stabilizing transition metals on specific carriers with defect sites, porous structures, or heteroatoms with lone pair electrons (such as N and S) is an effective method for preparing DSACs [27–30]. Based on precise control of composition and morphology, ideal ORR electrocatalysts can be obtained. The one-dimensional (1D) form of carbon carrier has the advantages of large specific surface area, good electronic conductivity, and adjustable porosity. It can expose many active sites, expand the pores of the material, and thus improve catalytic activity and stability [31–33]. Due to the unique coordination connection of MOFs, various metal and organic ligands can be paired with them. Therefore, MOFs can exhibit structures of various sizes, making them excellent N-C precursors for the preparation of DSACs [34–38].

Herein, Fe, Cu, and S were doped onto N-C nanorods derived from zeolitic imidazolate framework-8 (ZIF-8) to form co-doped hollow nanorod catalysts FeCuS-N-C with bimetallic active sites. The synergistic coupling of Fe and Cu bimetallic sites with N and S co-doping significantly regulates the electronic structure of Fe/Cu-Nx sites and improves the catalytic activity. Meanwhile, the one-dimensional carbon nanorods with high open pore structure and high conductivity can ensure effective exposure of active catalytic sites and enhance mass transfer performance. As expected, the synthesized FeCuS-N-C catalyst has excellent ORR activity, with an onset potential (E_{onset}) of 0.998 V and a half-wave potential ($E_{1/2}$) of 0.874 V. In addition, the catalyst also exhibits excellent stability, with a current density (it) stability of 98.21% after 10,000 s of testing, which is superior to the Pt/C materials currently on the market. Rechargeable ZABs assembled with FeCuS-N-C as the cathode material can achieve an open-circuit voltage (OCV) of up to 1.58 V, demonstrating excellent power density (105.2 mW cm^{-2}), specific capacity (807.4 mAh gZn^{-1}), and charge–discharge stability (over 250 h). Therefore, this study provides a new strategy for simultaneously adjusting the electronic and morphological structures of ORR DSAC electrocatalysts, offering a new approach for the manufacture of high-efficiency ZAB cathode materials.

2. Results and Discussion

2.1. Structural Characterization of the Catalysts

The preparation process of the hollow nanorod-shaped N, S-doped bimetallic catalyst FeCuS-N-C is shown in Figure 1. Firstly, the self templating method based on ZIF phase transition is used to break the Zn-N bond through heating. After completing the structural reconstruction, ZIF-L nanorods with hollow internal structures were prepared, which were then transformed into N-doped carbon hollow nanorods with perfectly replicated morphology [35]. Then, through a simple soaking and subsequent heat fixation process, a certain amount of Fe and Cu single atoms (about 1 wt%) with different proportions of S element were coordinated into N-doped carbon nanorods to obtain FeCuS-N-C hollow nanorods. It should be noted that this surface soaking process and the unique highly open hollow structure of the carbon framework can ensure that most isolated iron atoms are distributed on the surface of the carbon nanorod framework, thereby exposing the active sites of Fe/Cu-N$_4$ atoms.

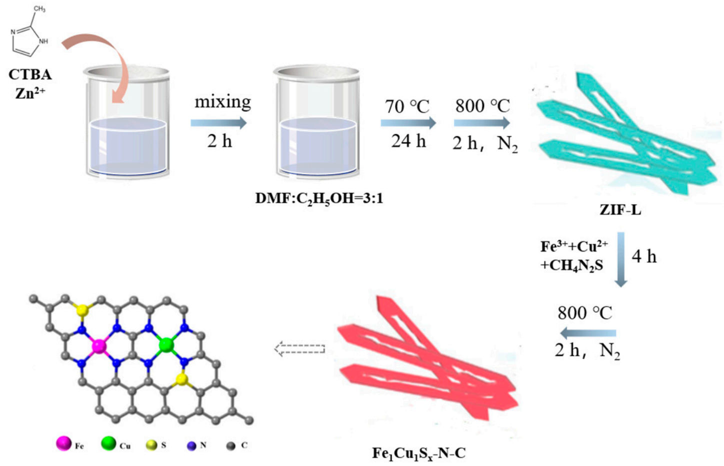

Figure 1. Illustration of the preparation of the electrocatalysts for Fe$_1$Cu$_1$S$_x$-N-C.

The elemental composition and morphology of the prepared catalyst were studied by scanning electron microscopy (SEM) (Figure 2). The SEM images clearly display the nanostructures of ZIF-8 and ZIF-L (Figure 2a,b). ZIF-L exhibits a uniform rod-shaped morphology, with a length of approximately 1 µm, which is different from the cubic shape of ZIF-8, indicating that the reaction in the mixed solution of N, N-dimethylformamide and ethanol changed the morphology of the sample. The morphology of Fe$_1$-N-C, Fe$_1$Cu$_1$-N-C, and Fe$_1$Cu$_1$S$_x$-N-C also exhibit nanorod-like morphology (Figure 2c–i). The results show that the doping of transition metals and heteroatoms does not affect the change of sample morphology. After two rounds of high-temperature pyrolysis, the morphology was also well preserved. The TEM image further confirms that Fe$_1$Cu$_1$S$_8$-N-C is in the form of nanorods, and crystalline metal nanoparticles are formed within the carbon matrix (Figure 2j,k). High-resolution TEM imaging shows that the size of crystalline metal nanoparticles is about 15–20 nm (Figure 2l). This one-dimensional nanorod structure can increase specific surface area of the catalyst, expose more active sites, and increase its contact area with the electrolyte. This improves the electrocatalytic activity and also provides a direct flow path, which shortens the charge–discharge time. The corresponding element mapping diagram show that C, N, O, S, Fe, and Cu elements are uniformly distributed in Fe$_1$Cu$_1$S$_8$-N-C (Figure 2m), indicating that Fe, Cu, and S elements have been successfully doped into the catalyst.

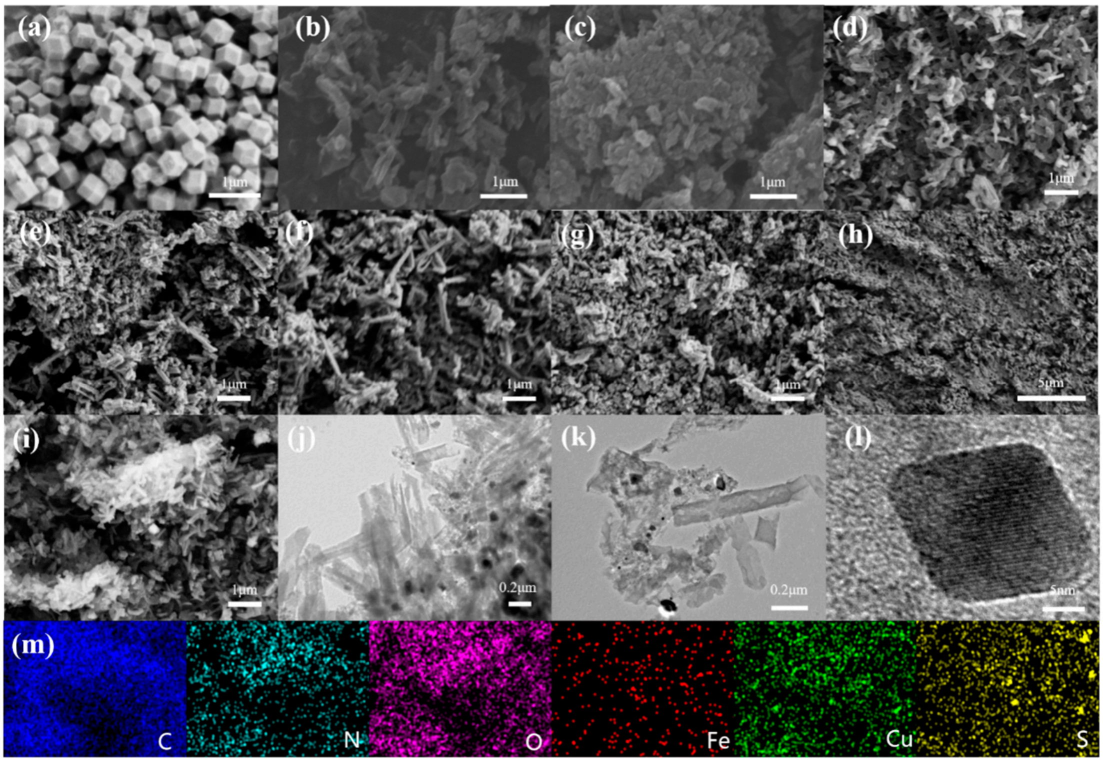

Figure 2. SEM image of (**a**) ZIF-8, (**b**) ZIF-L, (**c**) Fe_1-N-C, (**d**) Fe_1Cu_1-N-C, (**e**) $Fe_1Cu_1S_4$-N-C, (**f**) $Fe_1Cu_1S_{12}$-N-C, (**g**) $Fe_1Cu_1S_{16}$-N-C, (**h**,**i**) $Fe_1Cu_1S_8$-N-C; (**j**,**k**) TEM image of $Fe_1Cu_1S_8$-N-C, (**l**) HR-TEM image of $Fe_1Cu_1S_8$-N-C, and (**m**) elemental mapping images for $Fe_1Cu_1S_8$-N-C.

The prepared catalysts were analyzed by X-ray diffraction (XRD). The XRD patterns of Fe_1-N-C and Fe_1Cu_1-N-C (Figure 3) show two broad peaks near 24° and 44°, belonging to the (002) and (100) faces of graphite carbon, respectively [39]. $Fe_1Cu_1S_x$-N-C shows new diffraction peaks at 27.1°, 28.5°, and 47.5°, corresponding to the three components of S, Cu_8S_5, and FeS, respectively. As the content of thiourea in the reaction increased, the peak intensity of the three diffraction peaks also increased, indicating that the amount of the three components increased with the increase of S content, and also proving the successful doping of S element in the catalyst, which is consistent with the results of the element mapping. Meanwhile, since thiourea also provides an N source, the diffraction peak intensity representing the FeN at 3.61° increases accordingly [40]. The Cu_8S_5, FeS, and FeN can act as excellent active sites for the catalysts, helping to improve the ORR catalytic activity.

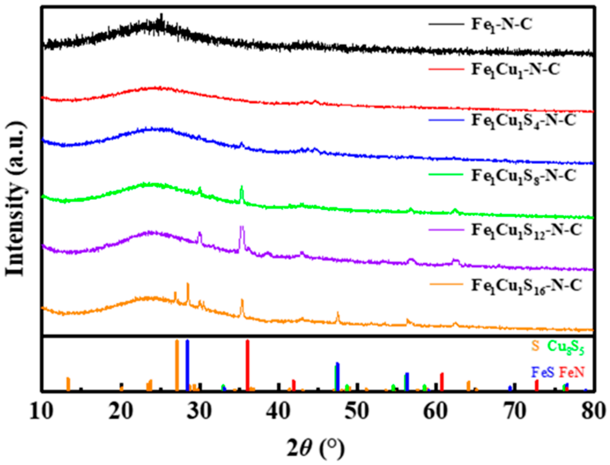

Figure 3. XRD patterns of $Fe_1Cu_1S_x$-N-C catalysts.

XPS was used to analyze the elemental composition and chemical valence state of the sample surface. The XPS spectra of Fe_1Cu_1-N-C and $Fe_1Cu_1S_8$-N-C are shown in Figure 4a. Fe_1Cu_1-N-C and $Fe_1Cu_1S_8$-N-C have similar peaks. In addition, $Fe_1Cu_1S_8$-N-C has an additional S 2p peak, which also proves the successful doping of Fe, Cu, and S elements into the catalyst. The results are consistent with the XRD and EDS element mappings. Figure 4b shows the comparison of C 1s XPS spectra between $Fe_1Cu_1S_8$-N-C and the Fe_1Cu_1-N-C. For the two catalysts, the binding energy is located at ~284.7 eV, ~285.6 eV, and ~289.0 eV, corresponding to C-C, C-N$_x$, and C-O/C=O structures [41], respectively. There is an additional fitted peak at ~286.2 eV in $Fe_1Cu_1S_8$-N-C, corresponding to the C-S bond [42], confirming that S element is doped into the $Fe_1Cu_1S_8$-N-C catalyst.

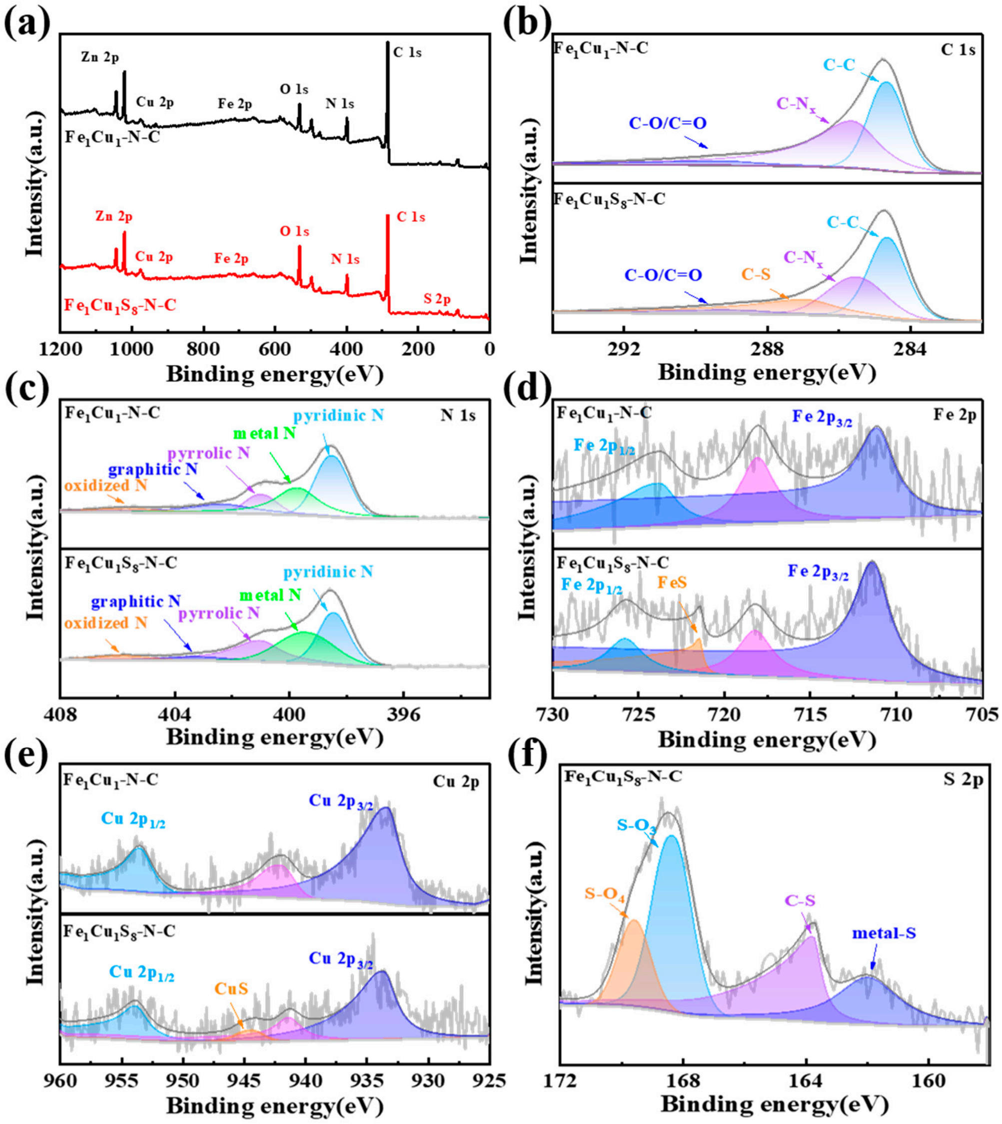

Figure 4. XPS spectra of Fe_1Cu_1-N-C and $Fe_1Cu_1S_8$-N-C catalysts. (**a**) Full survey spectra, (**b**) C1s, (**c**) N1s, (**d**) Fe 2p, (**e**) Cu 2p, and (**f**) S2p.

The N 1s XPS spectra of Fe_1Cu_1-N-C and $Fe_1Cu_1S_8$-N-C are shown in Figure 4c. The N 1s peaks of both catalysts exhibit four fitting peaks: pyridine-N (~398.5 eV), pyrrole-N (~400.3 eV), graphite-N (~402.7 eV), and oxidation-N (~404.0 eV). There is also an additional fitting peak at ~399.2 eV, corresponding to the metal-N$_x$ peaks of Fe-N$_x$ and Cu-N$_x$ [43–45]. The metal-N$_x$ structure can serve as the active sites of the catalysts.

Figure 4d shows the Fe 2p XPS spectra of Fe_1Cu_1-N-C and $Fe_1Cu_1S_8$-N-C. Compared with Fe_1Cu_1-N-C, the $Fe_1Cu_1S_8$-N-C sample not only has a Fe $2p_{3/2}$ fitting peak at ~710.7 eV and a Fe $2p_{1/2}$ fitting peak at ~724.2 eV [46,47], but also presents a fitting peak at ~718.7 eV, corresponding to the Fe-S structure [48]. The Cu 2p XPS spectrum in Figure 4e also shows that in addition to the Cu $2p_{3/2}$ (~933.7 eV) and Cu $2p_{1/2}$ (~953.5 eV) peaks, there is also a Cu-S (~944.7 eV) peak in the $Fe_1Cu_1S_8$-N-C sample [49,50]. Both Fe-S and Cu-S structures can serve as active sites for catalysts, indicating that $Fe_1Cu_1S_8$-N-C have more active sites compared to Fe_1Cu_1-N-C.

In the spectrum of S 2p in $Fe_1Cu_1S_8$-N-C (Figure 4f), the peak at 161.4 eV is the peak of metal sulfides, the peak at 163.8 eV is C-S, and the peaks at 168.0 eV and 169.2 eV are sulfur oxide peaks [51,52]. This also confirms that sulfur atoms have been successfully doped into carbon materials, and the metal-S and C-S structures have been confirmed to be active sites for improving ORR performance. From the XPS analysis, it can be seen that $Fe_1Cu_1S_8$-N-C has abundant C-N_x, and there are also graphite C, metal-N, and metal-S species as active sites, suggesting that the sample has excellent ORR performance.

2.2. Electrochemical Performances

The ORR performance of the FeCuS-N-C catalyst was evaluated due to its large specific surface area and abundant active sites. Firstly, the catalytic activity of all the samples was preliminarily evaluated by cyclic voltammetry (CV). As shown in Figure 5a, all catalytic materials exhibit oxygen reduction peaks in their CV curves under O_2 saturated 0.1 M KOH, while there is no oxidation peak under N_2 saturated environment. Among them, $Fe_1Cu_1S_8$-N-C has the highest oxygen reduction peak, indicating its best ORR catalytic performance among all catalytic materials. Accurate determination of ORR performance was performed using linear sweep voltammetry (LSV). Figure 5b shows the LSV test of ORR for various catalyst samples in a 0.1 M KOH solution saturated with O_2 at 1600 rpm. It can be seen that the initial potential (E_{onset} = 0.998 V) and half-wave potential ($E_{1/2}$ = 0.874 V) of $Fe_1Cu_1S_8$-N-C sample are significantly higher than those of other samples, and the E_{onset} and $E_{1/2}$ of Fe_1Cu_1-N-C samples are better than those of the Fe_1-N-C sample, indicating that the addition of Cu and thiourea improves the catalytic activity of the catalyst. See Table 1 for details. It is believed that the incorporation of S and N will induce the transition of spin polarization configuration for metal centers that act as the active site for oxygen reduction. This will promote the desorption of OH* species.

Table 1. The electrocatalytic performance of catalysts in 0.1 M KOH solution.

Samples	LSV		IT
	E_{onset}	$E_{1/2}$	
Fe_1-N-C	0.880 V	0.765 V	/
Fe_1Cu_1-N-C	0.924 V	0.816 V	97.32%
$Fe_1Cu_1S_4$-N-C	0.964 V	0.839 V	/
$Fe_1Cu_1S_{12}$-N-C	0.969 V	0.848 V	/
$Fe_1Cu_1S_{16}$-N-C	0.960 V	0.841 V	/
$Fe_1Cu_1S_8$-N-C	0.998 V	0.874 V	98.21%

To understand the ORR electron transfer pathway, the linear sweep voltammetry (LSV) curves of $Fe_1Cu_1S_8$-N-C at different rotational speeds (400~2025 rpm) were investigated (Figure 5c). The Koutecky–Levich (K–L) curve based on LSV curve has a good linear relationship in the range of 0.3~0.7 V, which conforms to the first-order reaction kinetics. The average electron transfer number (n) of $Fe_1Cu_1S_8$-N-C catalyst is 3.96, indicating that the majority of ORR catalytic reactions on the $Fe_1Cu_1S_8$-N-C catalyst follow a direct 4e transfer pathway. $Fe_1Cu_1S_8$-N-C not only has excellent ORR performance, but also has high stability. The stability of $Fe_1Cu_1S_8$-N-C and Fe_1Cu_1-N-C was studied through i-t testing. It was found that after continuous testing for 10,000 s, the stability of $Fe_1Cu_1S_8$-N-C remained around 98.21% under the condition of a current density of 5 mA cm^{-2}, which was better than the 97.32% of Fe$_1$Cu$_1$-N-C (Figure 5d), indicating that the doping of S element improved the stability of the catalyst.

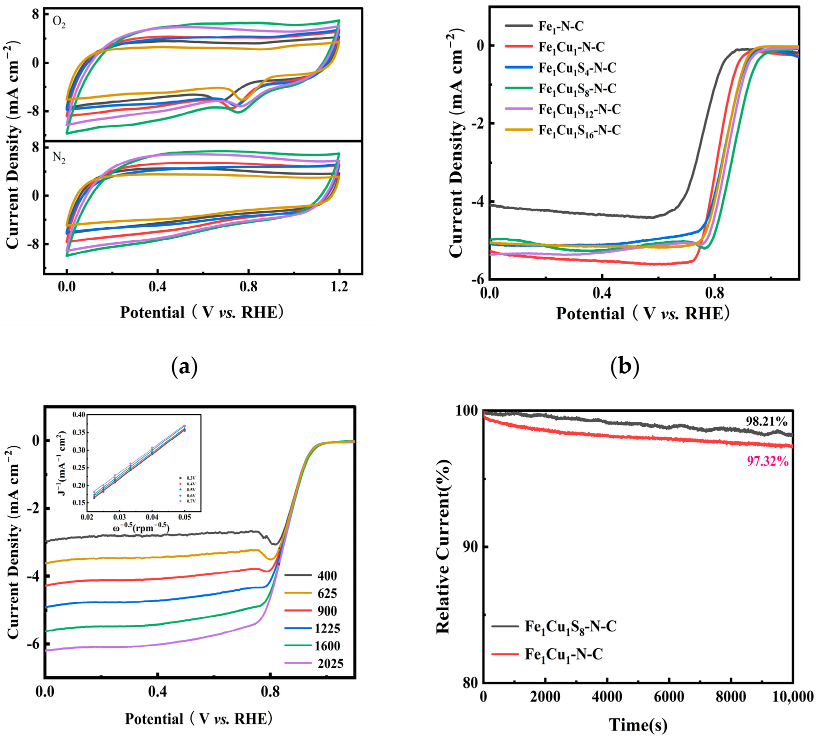

(**a**) (**b**)

(**c**) (**d**)

Figure 5. The electrocatalytic performance of catalysts in 0.1 M KOH solution. (**a**) CV curve, (**b**) ORR LSV diagram with a speed of 1600 rpm, (**c**) LSV curves of Fe$_1$Cu$_1$S$_8$-N-C at different rotational speeds, (**d**) IT stability curve.

2.3. Zn-Air Battery Performance

Considering the excellent ORR catalytic performance of the Fe$_1$Cu$_1$S$_8$-N-C catalyst, we constructed a self-made rechargeable ZAB and compared with the ZAB constructed from the control sample Fe$_1$Cu$_1$-N-C to evaluate its practical application. A self-made rechargeable ZAB was assembled using a carbon cloth supported catalyst as the air cathode, a zinc plate as the anode, and 6 M KOH solution containing 0.2 M Zn(Ac)$_2$ as the electrolyte.

As shown in Figure 6a, the open circuit voltage of the battery assembled with Fe$_1$Cu$_1$S$_8$-N-C is as high as 1.54 V, which is higher than the open circuit voltage of the zinc air battery assembled with Fe$_1$Cu$_1$-N-C (1.51 V). Subsequently, the peak power density of the zinc air battery assembled with two catalysts was compared (Figure 6b), and the Fe$_1$Cu$_1$S$_8$-N-C-based battery exhibited excellent peak power density, reaching up to 142.7 mW cm^{-2}, which was much higher than the Fe$_1$Cu$_1$-N-C-based battery (82.8 mW cm^{-2}). Based on the normalization of zinc quality, the specific capacity of Fe$_1$Cu$_1$S$_8$-N-C-based zinc air batteries reached 817.1 mAh gZn^{-1}, which also exceeded that of Fe$_1$Cu$_1$-N-C batteries (792.3 mAh gZn^{-1}) (Figure 6c). The battery assembled with Fe$_1$Cu$_1$-N-C exhibits a constant current charge–discharge cycle curve of over 250 h, indicating its high durability in zinc air batteries, while the constant current charge–discharge cycle curve of Fe$_1$Cu$_1$S$_8$-N-C-based batteries exceeds 400 h (Figure 6d,e), exhibiting more significant cycling stability than Fe$_1$Cu$_1$-N-C batteries. This excellent cycling stability indicates that Fe$_1$Cu$_1$S$_8$-N-C has potential application value in ZABs.

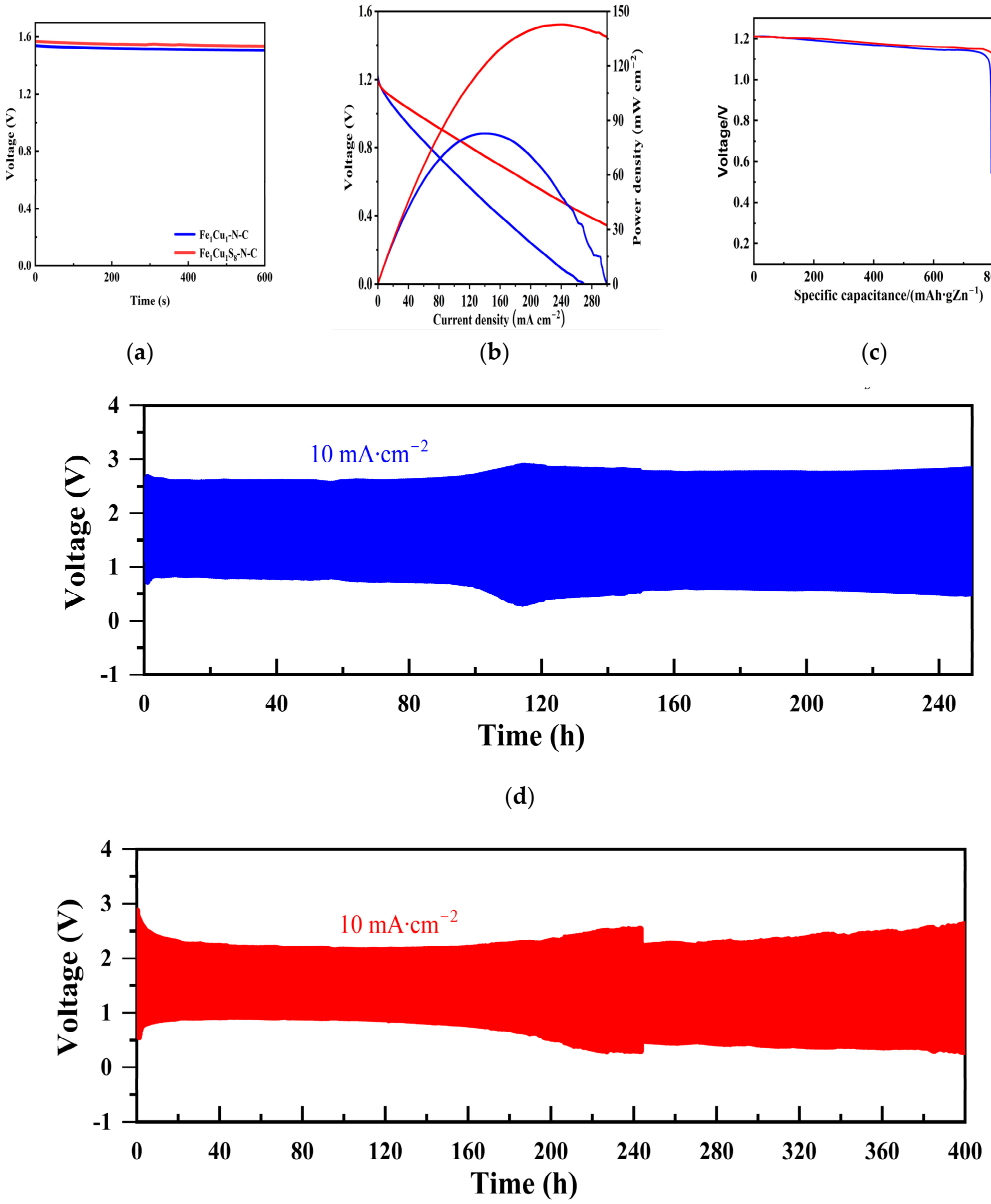

(**a**) (**b**) (**c**)

(**d**)

(**e**)

Figure 6. Electrochemical performance of flexible ZABs. (**a**) OCV curves, (**b**) discharge polarization curves and power density curves, (**c**) specific capacity curves at 20 mA cm^{-2}, Galvanostatic charge/discharge cycling curves of (**d**) Fe_1Cu_1-N-C and (**e**) $Fe_1Cu_1S_8$-N-C at 10 mA cm^{-2}.

3. Experimental Section

3.1. Chemicals

Hexadecyltrimethylammonium bromide ($C_{19}H_{42}BrN$, CTAB, Macklin, Shanghai, China), 2-Methylimidazole ($C_4H_6N_2$, Adamas, Shanghai, China), Nafion (5%, Alfa Aesar, Shanghai, China), Nine hydrated iron nitrate ($Fe(NO_3)_3 \cdot 9H_2O$, Sinopharm, Shanghai, China), copper nitrate trihydrate ($Cu(NO_3)_2 \cdot 3H_2O$, Sinopharm, Shanghai, China), zinc nitrate hexahydrate ($Zn(NO_3)_2 \cdot 6H_2O$, Sinopharm, Shanghai, China), thiourea (CH_4N_2S, Sinopharm, Shanghai, China), N, N-dimethylformamide (AR, Sinopharm, Shanghai, China), isopropanol (HPLC, Sinopharm, Shanghai, China), potassium hydroxide (AR, Sinopharm, Shanghai, China), and anhydrous ethanol (AR, Sinopharm, Shanghai, China) were used as starting materials.

3.2. Synthesis of Materials

3.2.1. Preparation of ZIF-L

Masses of 2 g $Zn(NO_3)_2{\cdot}6H_2O$, 3 g $C_4H_6N_2$, and 50 mg CTAB were added into 200 mL of deionized water. The system was then stirred at room temperature for 2 h. Subsequently, the solution was filtered and the solids were washed with deionized water. The collected white solids were added into a mixed solution of 120 mL N, N-dimethylformamide and 40 mL ethanol, and the solution was stirred at 70 °C for 2 h. The solution was then filtered, the solids were thoroughly washed with water, and the obtained solids were heated to 800 °C at 5 °C/min in a tube furnace under the protection of high purity nitrogen. White solid ZIF-L was obtained.

3.2.2. Preparation of $Fe_1Cu_1S_8$-N-C

Masses of 100 mg of ZIF-L, 10 mg of $Fe(NO_3)_3{\cdot}9H_2O$, 5 mg of $Cu(NO_3)_2{\cdot}3H_2O$, and 14 mg of CH_4N_2S were dissolved in isopropanol. The solution was stirred at room temperature for 2 h. The solution was filtered and the collected solids were dried to obtain $Fe_1Cu_1S_8$-ZIF-L. The $Fe_1Cu_1S_8$-ZIF-L was heated to 800 °C at 5 °C/min in a tube furnace under the protection of high purity nitrogen. $Fe_1Cu_1S_8$-N-C was obtained.

3.2.3. Preparation of Comparison Samples

Comparison samples of Fe_1Cu_1-N-C, $Fe_1Cu_1S_4$-N-C, $Fe_1Cu_1S_{12}$-N-C, and $Fe_1Cu_1S_{16}$-N-C were obtained according to the procedure mentioned in Section 3.2.2, where the mass of CH_4N_2S was replaced by 0, 7, 21, and 28 mg, respectively. Similarly, Fe_1-N-C was obtained by without adding CH_4N_2S and $Cu(NO_3)_2{\cdot}3H_2O$.

3.3. Characterization

Crystal phase and specific composition of the synthesized catalysts were characterized by X-ray diffractometer (XRD, Bruker D-8, Billerica, Massachusetts, Germany, Cu Kα, $\lambda = 1.5418$ Å) with a scanning rate of 7° min^{-1} and range of 2θ 10~80°. Morphology, microstructure, and element distribution of the catalysts were characterized by scanning electron microscopy (SEM, JSM-6480, JEOL, Akishima, Tokyo, Japan) and transmission electron microscopy (HRTEM, JEM-200CX, JEOL, Akishima, Tokyo, Japan). Surface element composition and bonding status of the catalysts were characterized by X-ray photoelectron spectroscopy (XPS, PHI 5000, ULVAC-PHI, Chigasaki, Japan, Al Kα).

3.4. Electrochemical Measurements

All electrochemical measurements were conducted on the CHI 730E electrochemical workstation using a three-electrode system at room temperature. The preparation of catalyst suspension in this work is as follows: 95 μL 5 wt% Nafion solution and 350 μL ethanol are added to every 10 mg of catalyst and mixed in a glass bottle, then ultrasonic treatment is performed, and the mixture is stirred for a total of 1 h. Then, a 4.5 μL catalyst suspension is dropped onto the surface of the GC electrode (~0.8 mg/cm^2), with a saturated $Hg/HgCl_2$ electrode (SCE) and a carbon rod as the reference electrode and counter electrode, respectively. All electrode potentials are converted to reversible hydrogen electrode potentials (RHEs) by correcting the equation $E_{RHE} = E_{SCE} + 0.244 + 0.0591 \times pH$. In the ORR test, N_2 (or O_2) is bubbled through the electrolyte for 30 min and kept bubbling during the measurement period to maintain N_2 or O_2 saturation in the solution. In a 0.1 M KOH solution, the cyclic voltammetry (CV) curve at 50 mV/s and the linear sweep voltammetry (LSV) at 10 mV/s are recorded at 400 to 2025 rpm and 0–1.2 V (ERHE). The final LSV curve is obtained by subtracting the background current measured in the N_2 purified electrolyte from the background current measured in the O_2-saturated electrolyte. According to the Koutecky–Levich equation, the electron transfer number n and dynamic current density J_K are calculated:

$$\frac{1}{J} = \frac{1}{J_L} + \frac{1}{J_K} = \frac{1}{B\omega^{1/2}} + \frac{1}{J_K}$$

$$B = 0.62nFC_0(D_0)^{2/3}\upsilon^{-1/6}$$

where J is the measured current; J_L is the diffusion limit current; ω is the angular velocity of the disk; F is the Faraday constant (96485 C mol^{-1}); C_0 is the volumetric concentration of oxygen (1.2×10^{-6} mol cm^{-1}); D_0 is the diffusion coefficient of oxygen (1.9×10^{-5} cm^2 s^{-1}); υ Is the dynamic viscosity (0.01 cm^2 s^{-1} at 0.1 M KOH); and n is the number of electrons transferred during the ORR process.

3.5. Zn-Air Battery Test

For the liquid ZABs, the anode is a polished 0.5 mm thick zinc sheet, the air cathode is a carbon cloth loaded with a catalyst, and the electrolyte is a 6.0 M KOH aqueous solution containing 0.2 M $Zn(Ac)_2$. The preparation method of cathode electrode catalyst ink is as follows: the 5 mg catalyst was added to a mixture of 200 μL water, 200 μL ethanol, and 40 μL 5 wt% Nafion solution, followed by ultrasonic treatment and stirring for a total of 1 h. The mass load of the active substance was approximately 2 mg cm^{-2}. The open circuit voltage, discharge polarization curve, and power density curve of the battery were measured on the electrochemical workstation (CHI 730E).

Using the Land 3001A battery test system, the constant current charge–discharge cycle curve and specific capacity of the battery were tested at room temperature. In each constant current cycle, the zinc-air battery was discharged for 10 min and charged for 10 min at a current density of 10 mA cm^{-2}. At the same time, the specific capacity was tested at the current density of 20 mA cm^{-2}.

4. Conclusions

Firstly, the self template method based on ZIF phase transition was used to prepare ZIF-L hollow nanorods as carbon substrates. Then, one-dimensional MOF-supported N, S co-doped bimetallic active site oxygen electrocatalyst FeCuS-N-C was prepared through two high-temperature pyrolysis processes. The catalyst exhibits good electrochemical performance (E_{onset} = 0.998 V, $E_{1/2}$ = 0.874 V) and stability. When used as a cathode catalyst for liquid ZAB batteries, it also exhibits excellent catalytic ability and has the highest power density, which is up to 142.7 mW cm^{-2} and a specific capacity of 817.1 mAh gZn^{-1}, and it can pass long-term cycle stability testing for over 400 h. The reasons why this catalyst has excellent ORR performance are: (1) Its highly hollow structure ensures effective exposure of active catalytic sites. (2) The morphology of one-dimensional carbon nanorods determines their high conductivity and rapid mass transport. (3) The doping of S element can regulate the electronic structure of Fe/Cu-N_4 active sites, thereby significantly reducing the energy barrier of the four-electron transfer step in the ORR process. This study provides an innovative approach for designing and optimizing non-precious metal catalysts for zinc air batteries.

Author Contributions: Conceptualization, methodology, validation, funding acquisition, H.S. and L.W.; investigation, formal analysis, Q.Z.; conceptualization, methodology, investigation, formal analysis, writing—original draft, W.S.; investigation, formal analysis, Y.Z.; conceptualization, methodology, validation, C.L.; conceptualization, methodology, validation, writing—review and editing, funding acquisition, R.Z. All authors have read and agreed to the published version of the manuscript.

Funding: This work has been financially supported by the Natural Science Foundation of Jilin Province, China, 2024 (YDZJ202401540ZYTS).

Data Availability Statement: The original contributions presented in the study are included in the article/Supplementary Materials, further inquiries can be directed to the corresponding author.

Conflicts of Interest: The authors declare that they have no known competing financial interests or personal relationships that could have appeared to influence the work reported in this paper.

References

1. Zhang, H.M.; Zhao, Y.; Zhang, Y.J.; Zhang, M.H.; Cheng, M.S.; Yu, J.L.; Liu, H.C.; Ji, M.W.; Zhu, C.Z.; Xu, J. Fe_3O_4 encapsulated in porous carbon nanobowls as efficient oxygen reduction reaction catalyst for Zn-air batteries. *Chem. Eng. J.* **2019**, *375*, 9. https://doi.org/10.1016/j.cej.2019.122058.
2. Quan, Y.W.; Zeng, K.; Meng, J.Q.; Jiang, D.Q.; Li, J.; Sun, X.Y.; Liu, H.T. Engineering cost-efficient CoS-based electrocatalysts for rechargeable Zn-air battery application. *Ind. Eng. Chem. Res.* **2023**, *62*, 6032–6038. https://doi.org/10.1021/acs.iecr.3c00300.
3. Ding, R.; Liu, Y.D.; Rui, Z.Y.; Li, J.; Liu, J.G.; Zou, Z.G. Facile grafting strategy synthesis of single-atom electrocatalyst with enhanced ORR performance. *Nano Res.* **2020**, *13*, 1519–1526. https://doi.org/10.1007/s12274-020-2768-y.
4. Zhang, W.; Zhang, J.W.; Wang, N.; Zhu, K.R.; Yang, C.C.; Ai, Y.; Wang, F.M.; Tian, Y.; Ma, Y.Z.; Ma, Y.; et al. Two-electron redox chemistry via single-atom catalyst for reversible zinc-air batteries. *Nat. Sustain.* **2024**, *7*, 463–473. https://doi.org/10.1038/s41893-024-01300-2.
5. Bu, M.M.; Liu, Y.; Liao, S.X.; Liu, W.J.; Yang, Z.H.; Jiang, J.B.; Gao, X.H.; Yang, Y.H.; Liu, H.T. In-site grown carbon nanotubes connecting Fe/Cu-N-C polyhedrons as robust electrocatalysts for Zn-air batteries. *Carbon* **2023**, *214*, 9. https://doi.org/10.1016/j.carbon.2023.118365.
6. Xu, L.; Wu, S.Q.; He, X.Y.; Wang, H.; Deng, D.J.; Wu, J.C.; Li, H.N. Interface engineering of anti-perovskite Ni3FeN/VN heterostructure for high-performance rechargeable Zinc-air batteries. *Chem. Eng. J.* **2022**, *437*, 9. https://doi.org/10.1016/j.cej.2022.135291.
7. Qi, C.H.; Yang, H.Y.; Sun, Z.Q.; Wang, H.F.; Xu, N.; Zhu, G.H.; Wang, L.J.; Jiang, W.; Yu, X.Q.; Li, X.P.; et al. Modulating electronic structures of iron clusters through orbital rehybridization by adjacent single copper sites for efficient oxygen reduction. *Angew. Chem.-Int. Edit.* **2023**, *62*, 11. https://doi.org/10.1002/anie.202308344.
8. Zhang, X.P.; Chandra, A.; Lee, Y.M.; Cao, R.; Ray, K.; Nam, W. Transition metal-mediated O-O bond formation and activation in chemistry and biology. *Chem. Soc. Rev.* **2021**, *50*, 4804–4811. https://doi.org/10.1039/d0cs01456g.
9. Xie, L.S.; Zhang, X.P.; Zhao, B.; Li, P.; Qi, J.; Guo, X.N.; Wang, B.; Lei, H.T.; Zhang, W.; Apfel, U.P.; et al. Enzyme-inspired iron porphyrins for improved electrocatalytic oxygen reduction and evolution reactions. *Angew. Chem.-Int. Edit.* **2021**, *60*, 7576–7581. https://doi.org/10.1002/anie.202015478.
10. Wu, Z.X.; Gao, Y.X.; Wang, Z.X.; Xiao, W.P.; Wang, X.P.; Li, B.; Li, Z.J.; Liu, X.B.; Ma, T.Y.; Wang, L. Surface-enriched ultrafine Pt nanoparticles coupled with defective CoP as efficient trifunctional electrocatalyst for overall water splitting and flexible Zn-air battery. *Chin. J. Catal.* **2023**, *46*, 36–47. https://doi.org/10.1016/s1872-2067(22)64198-6.
11. Zhang, F.; Ji, R.J.; Zhu, X.Y.; Li, H.K.; Wang, Y.T.; Wang, J.P.; Wang, F.; Lan, H.B. Strain-regulated Pt-NiO@Ni sub-micron particles achieving bifunctional electrocatalysis for Zinc-air battery. *Small* **2023**, *19*, 11. https://doi.org/10.1002/smll.202301640.
12. Weng, P.X.; Guo, Y.Q.; Wu, K.; Wang, X.; Huang, G.Q.; Lei, H.; Yuan, Y.F.; Lu, W.G.; Li, D. Design of Fe/Ni-doped N/S-rich carbon with advanced bifunctional electrocatalysis for Zn-air batteries. *J. Mater. Chem. A* **2023**, *11*, 12194–12201. https://doi.org/10.1039/d3ta01348k.
13. Zhang, W.; Xu, C.H.; Zheng, H.; Li, R.; Zhou, K. Oxygen-rich cobalt-nitrogen-carbon porous nanosheets for bifunctional oxygen electrocatalysis. *Adv. Funct. Mater.* **2022**, *32*, 8. https://doi.org/10.1002/adfm.202200763.
14. Tu, H.L.; Zhang, H.X.; Song, Y.H.; Liu, P.Z.; Hou, Y.; Xu, B.S.; Liao, T.; Guo, J.J.; Sun, Z.Q. Electronic asymmetry engineering of Fe-N-C electrocatalyst via adjacent carbon vacancy for boosting oxygen reduction reaction. *Adv. Sci.* **2023**, 10.1002/advs.202305194, 11. https://doi.org/10.1002/advs.202305194.
15. Mei, Z.Y.; Cai, S.; Zhao, G.F.; Zou, X.X.; Fu, Y.; Jiang, J.W.; An, Q.; Li, M.; Liu, T.T.; Guo, H. Boosting the ORR active and Zn-air battery performance through ameliorating the coordination environment of iron phthalocyanine. *Chem. Eng. J.* **2022**, *430*, 9. https://doi.org/10.1016/j.cej.2021.132691.
16. Zhou, Y.; Xing, Y.F.; Wen, J.; Ma, H.B.; Wang, F.B.; Xia, X.H. Axial ligands tailoring the ORR activity of cobalt porphyrin. *Sci. Bull.* **2019**, *64*, 1158–1166. https://doi.org/10.1016/j.scib.2019.07.003.
17. Zhang, J.; Zhang, J.J.; He, F.; Chen, Y.J.; Zhu, J.W.; Wang, D.L.; Mu, S.C.; Yang, H.Y. Defect and doping Co-engineered non-metal nanocarbon ORR electrocatalyst. *Nano-Micro Lett.* **2021**, *13*, 30. https://doi.org/10.1007/s40820-020-00579-y.
18. Li, Y.; Liu, X.; Zheng, L.; Shang, J.; Wan, X.; Hu, R.; Guo, X.; Hong, S.; Shui, J. Preparation of Fe–N–C catalysts with FeNx (x = 1, 3, 4) active sites and comparison of their activities for the oxygen reduction reaction and performances in proton exchange membrane fuel cells. *J. Mater. Chem. A* **2019**, *7*, 26147–26153. https://doi.org/10.1039/C9TA08532G.
19. Liao, S.X.; Huang, T.Q.; Wu, W.Y.; Yang, T.; Hou, Q.Q.; Sang, S.B.; Liu, K.Y.; Yang, Y.H.; Liu, H.T. Engineering high-entropy duel-functional nanocatalysts with regulative oxygen vacancies for efficient overall water splitting. *Chem. Eng. J.* **2023**, *471*, 8. https://doi.org/10.1016/j.cej.2023.144506.
20. Huang, Y.P.; Liu, K.; Kan, S.T.; Liu, P.G.; Hao, R.; Liu, W.F.; Wu, Y.F.; Liu, H.T.; Liu, M.; Liu, K.Y. Highly dispersed Fe-Nx active sites on Graphitic-N dominated porous carbon for synergetic catalysis of oxygen reduction reaction. *Carbon* **2021**, *171*, 1–9. https://doi.org/10.1016/j.carbon.2020.09.010.
21. Han, J.X.; Meng, X.Y.; Lu, L.; Bian, J.J.; Li, Z.P.; Sun, C.W. Single-atom Fe-Nx-C as an efficient electrocatalyst for Zinc-air batteries. *Adv. Funct. Mater.* **2019**, *29*, 8. https://doi.org/10.1002/adfm.201808872.

22. Li, L.F.; Chen, B.L.; Zhuang, Z.Y.; Nie, J.; Ma, G.P. Core-double shell templated Fe/Co anchored carbon nanospheres for oxygen reduction. *Chem. Eng. J.* **2020**, *399*, 9. https://doi.org/10.1016/j.cej.2020.125647.
23. Xu, X.L.; Zhang, X.M.; Kuang, Z.C.; Xia, Z.X.; Rykov, A.I.; Yu, S.S.; Wang, J.H.; Wang, S.L.; Sun, G.Q. Investigation on the demetallation of Fe-N-C for oxygen reduction reaction: The influence of structure and structural evolution of active site. *Appl. Catal. B-Environ.* **2022**, *309*, 9. https://doi.org/10.1016/j.apcatb.2022.121290.
24. Sun, J.; Xue, H.; Lu, L.L.; Gao, M.B.; Guo, N.K.; Song, T.S.; Dong, H.L.; Zhang, J.W.; Wu, L.M.; Wang, Q. Atomic-level modulation of local coordination environment at Fe single-atom sites for enhanced oxygen reduction. *Appl. Catal. B-Environ.* **2022**, *313*, 10. https://doi.org/10.1016/j.apcatb.2022.121429.
25. Wu, L.M.; Zhao, R.G.; Du, G.; Wang, H.; Hou, M.C.; Zhang, W.; Sun, P.C.; Chen, T.H. Hierarchically porous Fe/N/S/C nanospheres with high-content of Fe-Nx for enhanced ORR and Zn-air battery performance. *Green Energy Environ.* **2023**, *8*, 1693–1702. https://doi.org/10.1016/j.gee.2022.03.014.
26. Wu, Y.Y.; Ye, C.C.; Yu, L.; Liu, Y.F.; Huang, J.F.; Bi, J.B.; Xue, L.; Sun, J.W.; Yang, J.; Zhang, W.Q.; et al. Soft template-directed interlayer confinement synthesis of a Fe-Co dual single-atom catalyst for Zn-air batteries. *Energy Storage Mater.* **2022**, *45*, 805–813. https://doi.org/10.1016/j.ensm.2021.12.029.
27. Cui, T.T.; Wang, Y.P.; Ye, T.; Wu, J.; Chen, Z.Q.; Li, J.; Lei, Y.P.; Wang, D.S.; Li, Y.D. Engineering dual single-atom sites on 2D ultrathin N-doped carbon nanosheets attaining ultra-low-temperature Zinc-air battery. *Angew. Chem.-Int. Edit.* **2022**, *61*, 10. https://doi.org/10.1002/anie.202115219.
28. Dey, G.; Jana, R.; Saifi, S.; Kumar, R.; Bhattacharyya, D.; Datta, A.; Sinha, A.S.K.; Aijaz, A. Dual single-atomic Co-Mn sites in metal-organic-framework-derived N-doped nanoporous carbon for electrochemical oxygen reduction. *ACS Nano* **2023**, *17*, 19155–19167. https://doi.org/10.1021/acsnano.3c05379.
29. Tong, M.; Sun, F.; Xie, Y.; Wang, Y.; Yang, Y.; Tian, C.; Wang, L.; Fu, H. Operando cooperated catalytic mechanism of atomically dispersed Cu−N4 and Zn−N4 for promoting oxygen reduction reaction. *Angew. Chem. Int. Ed.* **2021**, *60*, 14005–14012. https://doi.org/10.1002/anie.202102053.
30. Zhang, Q.; Kumar, P.; Zhu, X.; Daiyan, R.; Bedford, N.M.; Wu, K.-H.; Han, Z.; Zhang, T.; Amal, R.; Lu, X. Electronically modified atomic sites within a multicomponent Co/Cu composite for efficient oxygen electroreduction. *Adv. Energy Mater.* **2021**, *11*, 2100303. https://doi.org/10.1002/aenm.202100303.
31. Hang, X.X.; Xue, Y.D.; Cheng, Y.; Du, M.; Du, L.T.; Pang, H. From Co-MOF to CoNi-MOF to Ni-MOF: A facile synthesis of 1D micro-/nanomaterials. *Inorg. Chem.* **2021**, *60*, 13168–13176. https://doi.org/10.1021/acs.inorgchem.1c01561.
32. Wang, Y.; Liu, X.; Liu, J.X.; Al-Mamun, M.; Liew, A.W.C.; Yin, H.J.; Wen, W.; Zhong, Y.L.; Liu, P.R.; Zhao, H.J. Electrolyte effect on electrocatalytic hydrogen evolution performance of one-dimensional cobalt-dithiolene metal-organic frameworks: A theoretical perspective. *Acs Appl. Energy Mater.* **2018**, *1*, 1688–1694. https://doi.org/10.1021/acsaem.8b00174.
33. Wei, Q.L.; Xiong, F.Y.; Tan, S.S.; Huang, L.; Lan, E.H.; Dunn, B.; Mai, L.Q. Porous one-dimensional nanomaterials: Design, fabrication and applications in electrochemical energy storage. *Adv. Mater.* **2017**, *29*, 39. https://doi.org/10.1002/adma.201602300.
34. Song, D.M.; Hu, C.G.; Gao, Z.J.; Yang, B.; Li, Q.X.; Zhan, X.X.; Tong, X.; Tian, J. Metal-organic frameworks (MOFs) derived materials used in Zn-air battery. *Materials* **2022**, *15*, 29. https://doi.org/10.3390/ma15175837.
35. Liu, Z.Q.; Liang, X.Y.; Ma, F.X.; Xiong, Y.X.; Zhang, G.B.; Chen, G.H.; Zhen, L.; Xu, C.Y. Decoration of NiFe-LDH nanodots endows lower Fe-d band center of Fe1-N-C hollow nanorods as bifunctional oxygen electrocatalysts with small overpotential gap. *Adv. Energy Mater.* **2023**, *13*, 10. https://doi.org/10.1002/aenm.202203609.
36. Ma, J.L.; Liu, L.L.; Zhao, R.H.; Yuan, D.; Ning, X. MOF-derived porous carbon nanofiber assembly as high efficiency ORR electrocatalysts for Zinc-air batteries. *Chin. J. Polym. Sci.* **2023**, *41*, 1889–1901. https://doi.org/10.1007/s10118-023-3006-3.
37. Zou, L.; Wei, Y.; Hou, C.; Wang, M.; Wang, Y.; Wang, H.; Liu, Z.; Xu, Q. One-step synthesis of ultrathin carbon nanoribbons from metal-organic framework nanorods for oxygen reduction and Zinc-air batteries. *CCS Chem.* **2022**, *4*, 194–204.
38. Pan, X.; Zhu, Q.; Yu, K.; Yan, M.; Luo, W.; Tsang, S.C.E.; Mai, L. One-dimensional metal-organic frameworks: Synthesis, structure and application in electrocatalysis. *Next Mater.* **2023**, *1*, 100010. https://doi.org/10.1016/j.nxmate.2023.100010.
39. Chang, H.; Guo, Y.F.; Liu, X.; Wang, P.F.; Xie, Y.; Yi, T.F. Dual MOF-derived Fe/N/P-tridoped carbon nanotube as high-performance oxygen reduction catalysts for zinc-air batteries. *Appl. Catal. B-Environ.* **2023**, *327*, 12. https://doi.org/10.1016/j.apcatb.2023.122469.
40. Xu, X.L.; Zhang, X.M.; Xia, Z.X.; Sun, R.L.; Li, H.Q.; Wang, J.H.; Yu, S.S.; Wang, S.L.; Sun, G.Q. Solid phase microwave-assisted fabrication of Fe-doped ZIF-8 for single-atom Fe-N-C electrocatalysts on oxygen reduction. *J. Energy Chem.* **2021**, *54*, 579–586. https://doi.org/10.1016/j.jechem.2020.06.046.
41. Li, X.; Ni, L.; Zhou, J.; Xu, L.; Lu, C.; Yang, G.; Ding, W.; Hou, W. Encapsulation of Fe nanoparticles into an N-doped carbon nanotube/nanosheet integrated hierarchical architecture as an efficient and ultrastable electrocatalyst for the oxygen reduction reaction. *Nanoscale* **2020**, *12*, 13987–13995. https://doi.org/10.1039/D0NR02618B.
42. Liu, X.; Liu, Y.; Zhang, C.; Chen, Y.; Luo, G.; Wang, Z.; Wang, D.; Gao, S. N, S co-doped hollow carbon nanocages confined Fe, Co bimetallic sites for bifunctional oxygen electrocatalysis. *Chem. Eng. J.* **2023**, *473*, 145135. https://doi.org/10.1016/j.cej.2023.145135.
43. Wang, Y.; Cui, X.; Peng, L.; Li, L.; Qiao, J.; Huang, H.; Shi, J. Metal–nitrogen–carbon catalysts of specifically coordinated configurations toward typical electrochemical redox reactions. *Adv. Mater.* **2021**, *33*, 2100997. https://doi.org/10.1002/adma.202100997.

44. Liu, H.; Jiang, L.; Wang, Y.; Wang, X.; Khan, J.; Zhu, Y.; Xiao, J.; Li, L.; Han, L. Boosting oxygen reduction with coexistence of single-atomic Fe and Cu sites decorated nitrogen-doped porous carbon. *Chem. Eng. J.* **2023**, *452*, 138938. https://doi.org/10.1016/j.cej.2022.138938.
45. Zhou, Y.; Tao, X.; Chen, G.; Lu, R.; Wang, D.; Chen, M.-X.; Jin, E.; Yang, J.; Liang, H.-W.; Zhao, Y.; et al. Multilayer stabilization for fabricating high-loading single-atom catalysts. *Nat. Commun.* **2020**, *11*, 5892. https://doi.org/10.1038/s41467-020-19599-8.
46. Li, Y.-W.; Zhang, W.-J.; Li, J.; Ma, H.-Y.; Du, H.-M.; Li, D.-C.; Wang, S.-N.; Zhao, J.-S.; Dou, J.-M.; Xu, L. Fe-MOF-derived efficient ORR/OER bifunctional electrocatalyst for rechargeable Zinc–air batteries. *ACS Appl. Mater. Interfaces* **2020**, *12*, 44710–44719. https://doi.org/10.1021/acsami.0c11945.
47. Wang, L.; Zhang, L.; Ma, W.; Wan, H.; Zhang, X.; Zhang, X.; Jiang, S.; Zheng, J.Y.; Zhou, Z. In situ anchoring massive isolated Pt atoms at cationic vacancies of α-NixFe1-x(OH)2 to regulate the electronic structure for overall water splitting. *Adv. Funct. Mater.* **2022**, *32*, 2203342. https://doi.org/10.1002/adfm.202203342.
48. Wang, S.; Ren, L.; Zhang, G.; Gong, Y.; Guo, Q.; Yu, G. Synthesis of N/Fe/S-codoped cathode catalysts on gasification residue carbon for Zinc–air batteries. *Energy Fuels* **2024**, *38*, 4676–4688. https://doi.org/10.1021/acs.energyfuels.3c04344.
49. Zhao, Y.; Sun, Q.; Liu, X.; Li, D.; Xing, S. Cu/Co/CoS2 embedded in S,N-doped carbon as highly efficient oxygen reduction and evolution electrocatalyst for rechargeable zinc–air batteries. *Inorg. Chem. Front.* **2022**, *9*, 2917–2927. https://doi.org/10.1039/D1QI01605A.
50. Bao, L.; Bao, C.; Sun, Q.; Zou, J.; Liu, H.; Chen, H. Hierarchical porous carbon with N/S codoped bimetal as a high-efficiency oxygen reduction catalyst for rechargeable Zinc–air batteries. *Energy Fuels* **2023**, *37*, 19137–19146. https://doi.org/10.1021/acs.energyfuels.3c03497.
51. Chang, H.; Zhao, L.; Zhao, S.; Liu, Z.-L.; Wang, P.-F.; Xie, Y.; Yi, T.-F. Tuning interface mechanism of FeCo alloy embedded N,S-codoped carbon substrate for rechargeable Zn-air battery. *J. Energy Chem.* **2024**, *93*, 400–410. https://doi.org/10.1016/j.jechem.2024.02.044.
52. Tao, S.; Xiang, S.; Yu, Y.; Lan, H.; Liu, C.; Zhang, J. Regulating electron region of central Fe atom in iron phthalocyanine by N, S-doped carbon nanofibers as efficient oxygen reduction catalysts for high-performance Zn-air battery. *Carbon* **2024**, *220*, 118893. https://doi.org/10.1016/j.carbon.2024.118893.